Membrane-Free Alkali Metal-Iodide Battery with a Molten Salt

Juhan Lee,* Gleidys Monrrabal, Martins Sarma, Tobias Lappan, Yvonne Jasmin Hofstetter, Pavel Trtik, Steffen Landgraf, Wenjin Ding, Sumit Kumar, Yana Vaynzof, Norbert Weber,* and Tom Weier*

Batteries with liquid metal electrodes are attractive candidates for sustainable energy-storage applications due to low manufacturing cost and high recyclability. These batteries should be developed for lower operating temperature, higher cell voltage, and membrane-free cell configuration. Herein, a new type of a membrane-free cell relying on liquid alkali metals and iodide is demonstrated. As a proof-of-concept study, membrane-free alkali metal-iodide (A-AI) batteries are constructed by a facile cell assembly introducing current collectors, LiI–LiCl–KI–CsI salt mixture, and an insulator without relying on solid-state mediums for separating electrolytes. For the initial assembly, no active electrode materials are required since they are naturally formed during battery operation. Despite the unoptimized cell construction, the membrane-free A-AI batteries show promising electrochemical performance such as a reliable stability for 250 cycles. The cells are able to handle a high current density and show a relatively low self-discharge rate, which implies the possibility of an iodine-concentrated layer at the bottom of the cell. This is further supported by postmortem analyses using neutron radiography. X-ray photoemission spectroscopy is performed to identify the changes in the iodine concentration in the cell.

1. Introduction

The reversible redox reactions of alkali and alkaline earth metals have been considered as promising sources for anode materials in rechargeable battery systems.[1–3] For this application, these metals can provide high theoretical storage capacities

in the range of 200–4000 mAh g^{-1}, and their highly negative redox potential below -2.5 V versus standard hydrogen electrode (SHE) can lead to a high cell operating voltage. These characteristics can enable high specific energies, which are generally given in the unit Wh kg^{-1} for expressing the energy-storage performance per mass of active materials or the system's total mass. However, the development of rechargeable batteries with alkali and alkaline earth metals has been extremely challenging due to the formation of dendrites, causing safety, stability, and efficiency issues.[1,4,5] As a solution to dendrite formation, solid-state electrolytes can be used as an alternative to conventional electrolytes dissolved in aqueous or organic solvents. However, according to recent studies,[5–8] dendrites can still penetrate the solid-state electrolytes, and the solid-solid interface of such energy-storage systems may cause other issues such as limited electrochemical stability window and physical contact loss between the electrolyte and the metal.

Another effective approach for handling the dendrite formation is to employ liquid metal anodes.[9–14] At temperatures above 25 °C, the redox reactions of alkali and alkaline earth metals can be utilized in a molten state either in its pure metal form[13,15] or

J. Lee, G. Monrrabal, M. Sarma, T. Lappan, S. Landgraf, N. Weber, T. Weier
Institute of Fluid Dynamics
Helmholtz-Zentrum Dresden – Rossendorf
Bautzner Landstr. 400, 01328 Dresden, Germany
E-mail: J.Lee@hzdr.de; norbert.weber@hzdr.de; t.weier@hzdr.de

Y. J. Hofstetter, Y. Vaynzof
Chair for Emerging Electronic Technologies
Technical University of Dresden
Nöthnitzer Str. 61, 01187 Dresden, Germany

(iD) The ORCID identification number(s) for the author(s) of this article can be found under https://doi.org/10.1002/ente.202300051.

Y. J. Hofstetter, Y. Vaynzof
Institute for Emerging Electronic Technologies
Leibniz-Institute for Solid State and Materials Research Dresden
Helmholtzstraße 20, 01069 Dresden, Germany

P. Trtik
Laboratory for Neutron Scattering and Imaging
Paul Scherrer Institut
Forschungsstrasse 111, 5232 Villigen PSI, Switzerland

W. Ding, S. Kumar
Institute of Engineering Thermodynamics
German Aerospace Center (DLR)
Pfaffenwaldring 38-40, 70569 Stuttgart, Germany

**ADVANCED
SCIENCE NEWS**
www.advancedsciencenews.com

Energy Technology
Generation, Conversion, Storage, Distribution

www.entechnol.de

as alloys.[16,17] The liquid feature of these anodes is not only beneficial in terms of eliminating the source of the issues regarding the dendrite formations but also in terms of a long operation lifetime, facile scalability, and low complexity in materials.[9,10] Therefore, compared to the solid-state counterpart, liquid metal anodes are attractive due to the possibility of low manufacturing cost as well as high recyclability. Depending on the choice of cathode materials, electrolytes, and cell configurations, various types of rechargeable batteries with liquid metal anodes have been already reported. Despite the advantages mentioned before, one of the major limitations of some of these batteries is the low operating voltage (<1.5 V);[10] the latter is a critical handicap since the specific energy results from combined functions of the cell voltage and the specific capacity.

While most of the rechargeable batteries with liquid metal anodes offer a cell voltage below 1.5 V, some systems are known for providing higher cell potentials, such as liquid-metal batteries (LMB) based on the cathode elements like Te and Se (1.5–2.4 V),[14,18] sodium–sulfur (Na‖S) systems (1.8–2.1 V),[19,20] and sodium–nickel (Na‖NiCl$_2$) systems, also known as Zeolite Battery Research in Africa (ZEBRA) batteries (2.6 V).[15,21] Relying on alloying reactions, Te- or Se-based cathode systems can contribute to a moderately high cell voltage at the operating temperature of around 470 and 360 °C, respectively. However, high costs and the low abundance of these elements in earth's crust are major hindrances to successful applications of Te- or Se-based systems.[9] In that regard, LMBs with displacement salt electrolytes based on more abundant elements like Zn[22–25] and Pb[26–28] seem to be more promising for a broad range of applications. Due to the high melting points of molten salt electrolytes based on Zn and Pb, the typical operating temperature has been reported at around 500–600 °C. This temperature range can be advantageous for particular applications under harsh conditions.[29] However, for broader applications, it is generally desired to develop systems that can be operated at as low temperature as possible. This is due to the issues at high temperatures such as thermal energy loss and corrosion, as well as a need for thermal insulating materials.

Compared to LMBs with displacement salt electrolyte, Na‖S and ZEBRA batteries can be operated at lower temperatures around 270–350 °C.[19] In addition, the high cell voltages and the high abundance of S make Na‖S batteries very attractive for more widespread applications. However, the necessity to use solid-state ion-selective mediums, such as NASICON or beta-alumina, is a significant drawback. These mediums, in the form of separators, membranes, diaphragms, etc., can cause stability, safety, and efficiency issues, including additional production costs and the complexity of the cell design.

The operating temperature of rechargeable batteries with anodes based on alkali or alkaline earth metals can be further reduced by relying on flexible cathode chemistry from metal cations to halide reactions with the aid of solid-state ion-selective mediums. Recently, Spoerke et al.[30] have reported a new type of sodium battery that can be operated in the temperature range of 110–180 °C. This low temperature was enabled by employing an inorganic molten salt catholyte consisting of at least one sodium halide and at least one metal. Hence, their batteries can be labeled as Na‖NaX–MX, (M = metal other than Na, X = F, Cl, Br, or I); for instance, the systems like Na‖NaI–AlCl$_3$, Na‖NaI–AlBr$_3$, or Na‖NaI–GaCl$_3$ have been reported so far.[31–33] In virtue of the high operating voltage of around 3.2 V and the effective utilization of redox activities from both cations and anions in the molten salt, high specific energy of over 150 Wh kg^{-1} has been reported.[33]

Like Na‖S and ZEBRA batteries, Na‖NaX–MX cells also require solid-state ion-selective mediums; in the absence of the latter, for instance, in the case of Na‖NaI–AlCl$_3$ systems, Al cations in the molten salt will be irreversibly deposited on the anode. A battery without such solid membranes could drastically simplify cell designs and configurations. Furthermore, greatly improved reliability and safety could be delivered since the solid-state membranes are prone to malfunctioning.

Here, we report a proof-of-concept study for membrane-free alkali metal-iodide (A-AI, A = Li, Na, K, Rb, Cs) batteries that can provide a cell voltage above 2.7 V. The essential part of this new type of battery is the presence of at least one type of alkali metal cations and iodide anions in the molten salt. Other types of cations and anions can be added for enhancing the performance; however, cations with a reduction potential higher than −2.5 V versus SHE such as Al or Ga should not be introduced. We demonstrate the membrane-free operation of A-AI batteries by employing LiI–LiCl–KI–CsI molten salt at temperatures around 240–300 °C and discuss their key battery performance in terms of specific energy density, power handling performance, self-discharge rate, and cyclability.

The manuscript is structured as following: within Section 2, we describe the used methods, including materials, electrochemical characterization, differential scanning calorimetry (DSC), and postmortem analysis. Subsequently, we discuss the results in terms of cell performance of open and closed cells, the influence of cathode current collector and salt composition as well as self-discharge and long-term performance before concluding our results in Section 3.

2. Results and Discussion

2.1. Proof of Concept (Open Cell)

For demonstrating the proof of concept of our membrane-free A-AI batteries, an open-cell battery was assembled with a LiI–LiCl–KI–CsI electrolyte with a molar ratio of 54:10:9:27 or 58:5:9:28 as schematically illustrated in **Figure 1**A (left). These mixtures were chosen based on the low melting points (180–210 °C).[34–36] The presence of Cs in our salt mixture is not essential for the battery operation; hence, it can be excluded or replaced by other metal cations. However, for the simplicity of our proof-of-concept study, we involved Cs to employ its known role in reducing melting points in the alkali metal halide mixtures.

After heating the open-cell containing LiI–LiCl–KI–CsI with a molar ratio of 54:10:9:27 to 240 °C and 1 h of resting time, a galvanostatic charging/discharging cycle was applied at 100 mA cm^{-2} as normalized to the area of the cathode current collector under a full-cell configuration (Figure 1B). For the invested charge of 40 mAh g^{-1} normalized to the active materials, including the mass of the molten salt, the cell voltage profile (black line) shows a promising feature of our membrane-free
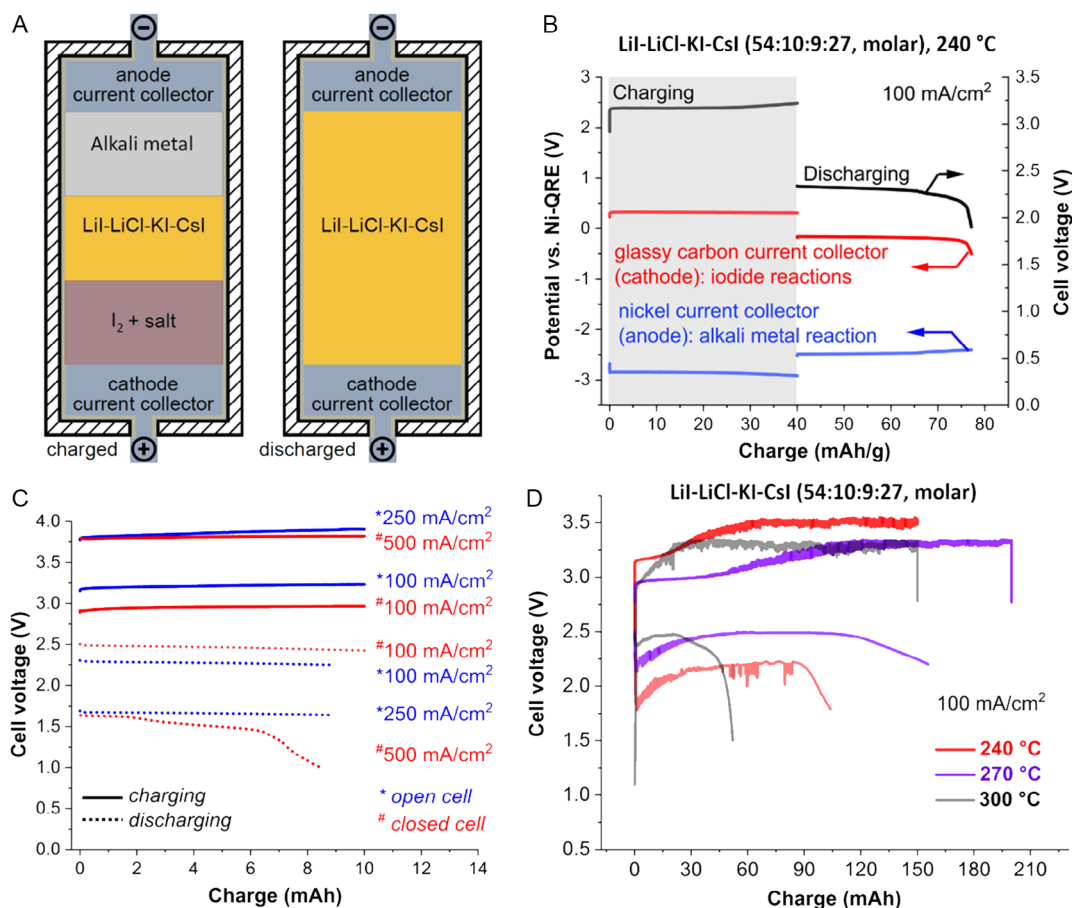
Figure 1. A) The schematic illustration of the membrane-free alkali metal-iodide (A-AI) batteries with molten salt and B–D) the characterization results of the open cells filled with LiI–LiCl–KI–CsI molten salt mixtures. B) Cell voltage profiles obtained during galvanostatic charging/discharging at 100 mA cm^{-2}. The potentials of the individual electrodes were recorded with the aid of a nickel quasi-reference electrode (Ni-QRE). C) Cell voltages profiles at various current densities: 100, 250, and 500 mA cm^{-2}. D) Cell voltage profiles obtained at various temperatures (240, 270, and 300 °C) at 100 mA cm^{-2}.

A-AI cell as supported by the energy efficiency of 67%, Coulombic efficiency of 93%, and the cell voltage around 2.7 V. In particular, the latter is the highest value among the reported membrane-free molten-salt batteries, and the second highest among the known molten-salt batteries to the best of our knowledge; the highest cell voltage reported so far is around 3.3 V for Na||NaX–MX batteries.[31]

While measuring the cell voltage, the individual potentials (Figure 1B) of the cathode (*red line*) and anode (blue line) were also recorded with the aid of the Ni-QRE as a spectator reference; the details of the spectator reference can be found elsewhere.[37–39] The reduction/oxidation potential plateaus at around −2.7 V versus Ni-QRE indicate the reversible reaction of the alkali metal cations, while the oxidation/reduction plateaus at around 0.1 V versus Ni-QRE indicate the reversible reaction of iodide. Hence, the major charge-storage mechanisms of our proof-of-concept cell can be summarized in the schematic illustration shown in Figure 1A; during charging, the metals float on the top of the liquid electrolyte while the iodine in the oxidized state sinks to the bottom of the liquid; the reverse reactions occur during discharging. These reactions can also be expressed as

$$\text{Anode}: A^+(l) + e^- \rightleftarrows A(l) \tag{1}$$

$$\text{Cathode}: I^-(l) \rightleftarrows 0.5 I_2(l) + e^- \tag{2}$$

For aqueous and organic electrolytes, reversible iodide reactions have been applied to various electrochemical applications,[38,40–42] and their reaction mechanisms have been explored from flat electrodes to highly porous materials.[43–45] Depending on the electrolytes and the electrodes, the reported reaction mechanisms vary; however, the formation of polyiodides, such as I_3^- and I_5^-, is generally accepted. Despite the well-established reaction mechanisms for alkali metal cations at the anode, the iodide reaction mechanisms in molten salt systems have not been well explored; yet, the presence of polyiodide has been reported from various studies regarding room-temperature molten salt systems.[46–48] Therefore, the polyiodides can possibly be formed during cell charging. However, understanding the detailed reaction mechanisms of iodine in our A-AI batteries is beyond the scope of our study.

To investigate the initial power handling performance, the test cell was further investigated (Figure 1C, blue-colored curves) by

**ADVANCED
SCIENCE NEWS**

www.advancedsciencenews.com

Energy Technology
Generation, Conversion, Storage, Distribution

www.entechnol.de

applying different current densities at 240 °C. At 100 mA cm^{-2}, the cell showed a moderate voltage efficiency of ≈71%; however, at a higher current density of 250 mA cm^{-2}, the voltage efficiency was reduced to 43%. Among other experimental variations, one of the most important parameters to test is the operating temperature. In that regard, an open-cell containing LiI–LiCl–KI–CsI with a molar ratio of 54:10:9:27 was tested at various fixed temperatures in the range of 240–300 °C (Figure 1D). The oscillations of the cell potential, which appear especially during the charge phase, are most probably caused by insufficient wetting of the anode current collector, and the formation of small alkali metal droplets.[49]

Based on the voltage profiles, increasing the operating temperature seems to be beneficial in terms of reducing the cell resistance; however, the low Coulombic efficiency of 35% indicates ineffective energy storage at 300 °C. Since the top of the cell was open to the environment, this ineffectiveness at the elevated temperature may be due to an increased self-discharge rate caused by strong thermal convection[50–52] or the high vapor pressure of liquid I_2.[46,53] With a boiling temperature of 184 °C, the latter might simply evaporate if not bound as triiodide species. Yet, despite the period of one charge/discharge cycle of around 110 min for the data shown in Figure 1D at 300 °C, the Coulombic efficiency of 35% indicates that the iodine does not rigorously boil out in the open cell. Furthermore, the Coulombic efficiency of 78% at 270 °C implies that the iodine would not boil despite the known boiling temperature of 184 °C but would rather slowly evaporate via the vapor pressure. In the latter case, the iodine would not evaporate in a closed-cell configuration when equilibrium is achieved.

2.2. Influence of Salt Composition, Current Collector, and Cell Sealing

One of the critical tasks for molten-salt battery systems is the optimization of the salt mixture. Hence, we have simulated various phase diagrams of the LiI–LiCl–KI–CsI mixture with 0, 5, and 10 mol% LiCl with the thermodynamic simulation software FactSage (**Figure 2**A, see also Figure S2, Supporting Information). Among them, the LiI–LiCl–KI–CsI mixture with 5 mol% LiCl is estimated to have the minimum melting temperature of 197 °C at the molar ratio of 58:5:9:28 (Figure 2A). Based on these simulated results, the composition that leads to the lowest melting temperature at each phase diagram was chosen for further experimental confirmation with DSC. The results are summarized in **Table 1** based on the onset temperature measured in the heating curve. As exemplified for the mixture with the molar ratio of 58:5:9:28 (Figure 2B), a peak with the onset temperature of 190 °C is observed in the heating curve, and a small secondary peak with the onset temperature of 354 °C exists. This means that the LiI–LiCl–KI–CsI salt mixture with the simulated eutectic composition of 58:5:9:28 mol% is very close to the real eutectic salt mixture.

Based on the DSC analysis and the major limitation of the open-cell configuration regarding the electrolyte evaporation, further cell characterization was carried out with the mixture with 58:5:9:28 mol% in the closed-cell configuration. Additionally, we employed a carbon felt (see Figure S3, Supporting Information
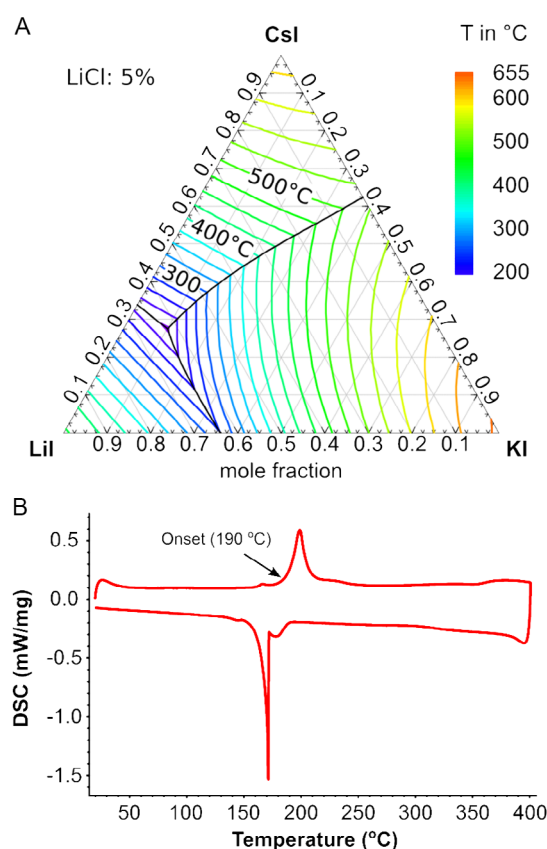

Figure 2. A) Simulated phase diagram of LiI–LiCl–KI–CsI mixture with 5 mol% LiCl with the thermodynamic simulation software FactSage. B) Differential scanning calorimetry (DSC) curves of LiI–LiCl–KI–CsI (58:5:9:28 mol%) eutectic mixture, which were measured with a salt sample of about 10 mg and a heating and cooling rate of 5 K min^{-1} under the Ar flow of 20 mL min^{-1}.

Table 1. Onset observed temperatures from DSC for various salt mixtures.

LiI–LiCl–Ki–CsI molar ratio	Onset in the heating curve [°C]
60:0:10:30	197
58:5:9:28	190
54:10:9:27	192

for the details) as current collectors since it is a common cell component of redox-flow batteries, where redox-active electrolytes, known as anolytes and catholytes, are utilized as active materials.[42,54] Compared to the flat electrodes, the felt structure is advantageous in our case, as it provides more surface area for the iodide reactions in the molten salt;[31] the latter works similarly to the catholytes in the redox flow batteries.[46,54]

The benefit of applying the carbon felt with the optimized electrolyte mixture can be seen from the power handling performance obtained at 240 °C, as shown in Figure 1C with red-colored curves. Compared to the performance of the open-cell configuration with the unoptimized mixture (LiI–LiCl–KI–CsI, 54:10:9:27 mol%), this cell configuration demonstrated significantly enhanced voltage efficiencies as indicated

**ADVANCED
SCIENCE NEWS**

www.advancedsciencenews.com

Energy Technology
Generation, Conversion, Storage, Distribution

www.entechnol.de

by the lower overvoltage. In this case, the enhancement could be contributed by the use of the porous carbon current collector and/or improved diffusion via the lower melting point of the optimized mixture (58:5:9:28 mol%). In particular, the battery cell was able to be operated at 500 mA cm^{-2} with a voltage efficiency of around 40%. This performance is comparable to other recently reported molten-salt batteries system,[55–57] and improvements are highly expected through further developments.

2.3. Electrochemical Characterization

At 240 °C, our closed cell was galvanostatically characterized at 50 mA cm^{-2} by limiting the charging time (**Figure 3**A). By varying the latter parameter, the cell was operated at different time scales for a charge/discharge cycle: 0.8, 3, and 5.8 h. As indicated by the close distance between the charging and discharging plateaus, the cell exhibited a high energy efficiency of 85% for 0.8 h operation time. For the longer operation time of 5.8 h, specific energy of 34.2 Wh kg^{-1} was measured with an energy efficiency of 59%. These results indicate that the tested cell system can be applied as a stationary energy-storage system where under 5 h charge/discharge period is required; for instance, as a facility for shaving three major peaks in electricity during a day.[58]

In fact, the expected theoretical specific energy is about 478 Wh kg^{-1} by considering the theoretical charge-storage capacity of 177 mAh g^{-1} for the LiI–LiCl–KI–CsI salt with a molar ratio of 58:5:9:28 and the cell voltage of 2.7 V; for simplicity, it is assumed that all alkali metal ions in the electrolyte contribute to the charge-storage reactions. Compared to many other high-temperature storage systems, including ZEBRA and Na∥S cells, this is a comparably high value. The specific energy value obtained from our proof-of-concept cell is about 7% of the theoretically expected value; however, the value of 34.2 Wh kg^{-1} is comparable to some of the other reported measured values.[57,59] Also, unlike other systems, our normalized values consider the mass of both active electrode materials and molten salt, while in most cases, the specific energy is reported based on the mass of the active electrode materials only. Furthermore, the maximum specific energy observed from our proof of concept is rather

limited due to the lack of optimization and cell engineering. Hence, the A-AI batteries have a promising potential for further improvements.

The specific energy achieved for the A-AI batteries could have been contributed from more than one reaction at the anode compartment due to the presence of Li, K, and Cs in the electrolyte. The possibility of multiple reactions at the anode compartment could be possibly implied by the presence of two evident plateaus in the discharging profile at constant current (see Figure S4A, Supporting Information) as well as by two clear dQ/dV peaks (Figure S4B, Supporting Information). During charging, the potential variation was not quite significant compared to that obtained during the discharging step, as evidenced by a flat voltage profile (Figure S4A, Supporting Information) and a single sharp peak obtained from dQ/dV analysis (Figure S4B, Supporting Information).

The standard redox potentials for Li/Li$^+$, Cs/Cs$^+$, and K/K$^+$ are about −3.04, −3.03, and −2.93 versus SHE; however, the actual redox potentials are expected to be different depending on the detailed conditions in the cell. Also, since the kinetics for these reactions will also vary, identifying the reactions from the measured voltage plateaus at constant current is not quite straightforward. Assuming that voltage plateaus are caused mostly by the reactions at the anode compartment, the plateau at the low potential range could be contributed by the potassium reaction just based on its standard redox potential and the least contribution for charge-storage capacity (See Figure S4A, Supporting Information); the theoretical value for the latter is 317 mAh for the salt mixture applied in the cell. Because of the importance of knowing the salt composition change during battery operation, investigating the detailed kinetics and thermodynamics of individual reactions is critical for the further development of the A-AI batteries. However, this is considered beyond the scope of this work.

2.4. Self-Discharge

Earlier, we observed a decrease in energy efficiency for 5.8 h of charge/discharge time compared to that for 0.8 and 3 h. This
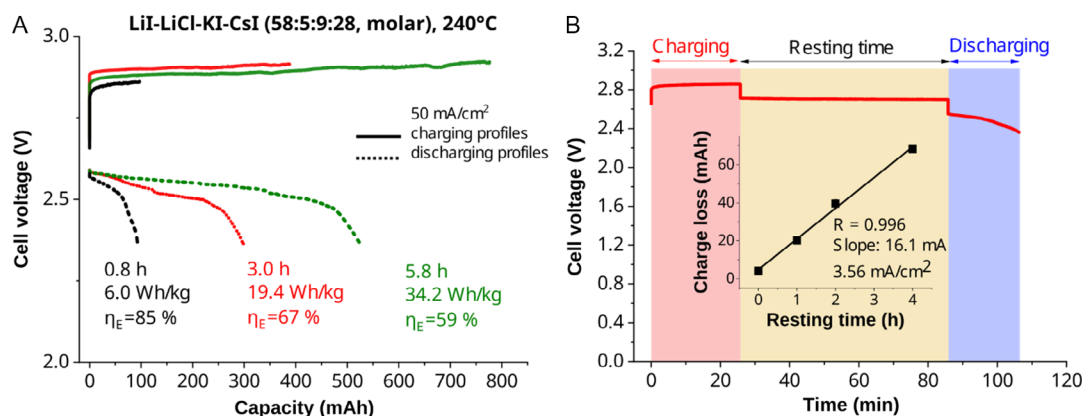

Figure 3. Electrochemical performance of membrane-free A-AI batteries with LiI–LiCl–KI–CsI molten salt with a molar ratio of 58:5:9:28. A) Cell voltage profiles obtained from galvanostatic charging/discharging at 50 mA cm^{-2}. Based on the profiles, specific energy (Wh kg^{-1}) and energy efficiency (η_E) values were calculated. B) Self-discharge rate analysis by applying various resting times after charging the cell. Inset shows the charge loss as a function of resting time. All results were obtained in the closed-cell configuration.

tendency can be explained by the decrease in Coulombic efficiency for longer charge/discharge time: 96%, 77%, and 68% for 0.8, 3.0, and 5.8 h, respectively. The Coulombic efficiency below 100% can be due to undesired reactions such as electrolyte and electrode decompositions as well as self-discharging phenomena. Because the experiments were carried out by increasing the charging time, the primary cause for the decreasing Coulombic efficiency seems to be self-discharge. The rate of the latter can be quantitatively determined by introducing various resting times between the charge/discharge operations. In our case, the cell was charged at $50 \, \mathrm{mA \, cm^{-2}}$, rested for 0, 1, 2, and 4 h, and subsequently discharged at $50 \, \mathrm{mA \, cm^{-2}}$ (Figure 3B). Then, the difference between the charge invested and charge regained, or the charge loss in mAh, is plotted as a function of the resting time (Figure 3B, inset). The slope of the fitted linear line represents the self-discharge rate of the cell, which was about 16.1 mA or $3.56 \, \mathrm{mA \, cm^{-2}}$ normalized to the cross-sectional area of the inner cell between the cathode and anodes. In the ideal case, the self-discharge rate of the molten salt systems should be below $1 \, \mathrm{mA \, cm^{-2}}$, which has been occasionally reported by advanced or well-optimized systems.[53,60,61] However, higher self-discharge rates can often be faced, in particular, by the molten salt systems based on sodium anodes.[10,59,61]

In fact, high self-discharge rates are one of the known challenges for molten salt systems as often caused by the high solubility of liquid metals in molten salt;[62] for instance, Li and Mg have been generally accepted for low solubility, while elements like Na and K are known for their high solubility.[9] For our A-AI batteries, another possible contribution to the self-discharge is the redox shuttling of iodide ions.[38,40,41,63] In traditional electrolyte systems with solvents, the iodine in the oxidized state at the cathode is transported to the anode and reduced back to iodide, which is similar to the case of self-discharge mechanisms for alkali metal anodes in molten salt systems. Unfortunately, the redox shuttling behavior of iodide for energy-storage systems with molten salt systems has not been explored yet. Nonetheless, considering the unique characteristics of molten salt electrolytes, it might be possible that iodide behaves differently in molten salts than in solvent-based conventional systems. For instance, despite the presence of a certain level of convection caused by inhomogeneous heating of the cell from the bottom without particular thermal insulators, the observed self-discharge rate of $3.56 \, \mathrm{mA \, cm^{-2}}$ indicates that the redox shuttling level of iodide seems to be significantly suppressed. The redox shuttling level can be further suppressed by improving the anode current collector design, applying porous separator, or filler materials between the anode and cathode compartment to avoid convection caused by thermal, solutal, or magneto-hydrodynamically induced effects.[12,24,41,43,52,64–68]

The relatively low level of self-discharge observed in our study implies that the iodine in the oxidized state tends to stay in the bottom layer of the molten salt, as described earlier in Figure 1A. After oxidation at the cathode current collector, iodine could be in the form of polyiodide or liquid I_2. While the former form is dissolved in the molten salt, the latter form may build a stable layer at the bottom of the cell due to the higher density of I_2 ($\approx 3.7 \, \mathrm{g \, cm^{-3}}$ at 240 °C) than the molten salt;[69] the densities of the molten LiI, LiCl, KI, and CsI are around 3.3, 1.7, 2.9, and $3.6 \, \mathrm{g \, cm^{-3}}$, respectively.[70] In the case of the dissolved

polyiodides, their higher density than that of iodide, I^-, may lead to their inhomogeneous distribution in the molten salt via gravitational influence, which eventually might lead to solutal convection, as well.[52,67,71–73] While the presence of polyiodide has been reported for room-temperature molten-salt systems,[46–48] the physical and chemical state of iodine in detail for the A-AI battery configuration has been unexplored so far.

2.5. Postmortem Analysis

To explore the physical and chemical state of iodine in the A-AI batteries, an open cell with a graphite crucible was charged up to 100 mAh at 200 mA at 240 °C, rested for 1 h, and cooled down to room temperature without applying particular cooling in the glove box. The inner diameter of the graphite crucible is 25.4 mm; cell geometry has been described in the Experimental Section. After cooling, the cell was cross sectioned by a band saw in air and subsequently stored in the glove box. The exposure time to air during the cutting process was controlled as short as possible to avoid the reaction of air with the salt and alkali metals.

The cross-sectioned sample is imaged in the Figure S5A, Supporting Information. A clear brownness gradient is evident: the sample is darker at the bottom and lighter at the top. The observable color is a typical characteristic of iodine and agrees with its tendency to remain at the bottom of the cell, as explained before in Figure 1A. In addition, higher iodine-concentrated spots are observable. One such feature, marked as "dark brown" spot in **Figure 4**A, has been investigated using XPS. The survey result (see Figure S5E, Supporting Information) indicates the presence of iodine as well as other elements, such as Li, Cs, K, Cl, O, and C. The two latter elements were possibly introduced during the storage and the sample preparation process or caused by some initial impurities in the cell system; hence, we exclude the contribution of O and C to the sample composition in the following analysis. The deconvoluted peaks located at 617.85 and 619.38 eV (Figure 4B) agree with the other reported binding energies from the iodide in salts and pure iodine.[74] According to the calculation, the atomic compositions showed a contribution of iodide (I^-) of 65.9% and of iodine (I_2) of 15.4%, leading to a total contribution of around 81% from this spot. In contrast, the measurement of a dark feature at the top, marked "dark" spot in Figure 4A, revealed around 46% contribution of iodine and 44% contribution of Li. These results align with the charge-storage mechanism explained earlier in Figure 1A. During the charging process, iodides in the salt are oxidized at the bottom part of the cell, while lithium cations in the salt are reduced at the upper part of the cell. The iodine-rich "dark brown" spot most likely forms at the bottom part of the cell during the cooling process, possibly, due to high iodine concentration after the charging process and the melting temperature difference between the molten salt and the iodine. Since redox shuttling is a diffusion-related phenomenon, confining iodine (I_2 and polyiodide) in a porous current collector such as carbon felt can be beneficial. Hence, an open cell with a graphite crucible with carbon felt was prepared following the same procedure described earlier; then, the cell was examined by neutron radiography. Due to higher neutron transmission of carbon than that of the salt mixture (area L_1), the

ADVANCED
SCIENCE NEWS
www.advancedsciencenews.com

Energy Technology
Generation, Conversion, Storage, Distribution
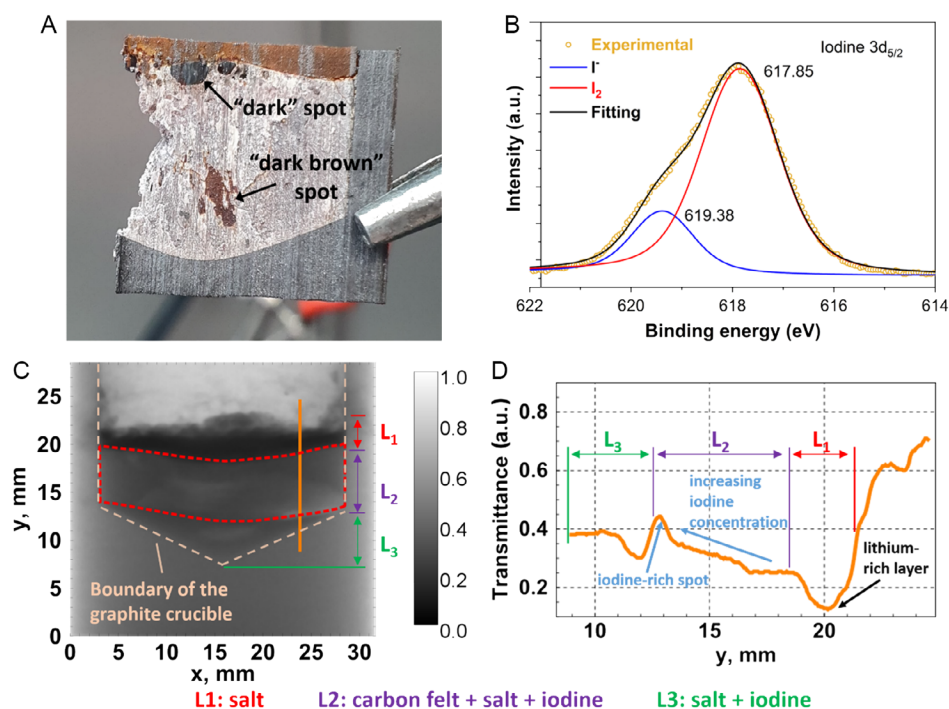www.entechnol.de

Figure 4. A,B) Postmortem analyses with X-ray photoemission spectroscopy (XPS) and C,D) neutron radiography. A) A slice of the investigated postmortem battery cell with no carbon felt applied. B) XPS spectrum of iodine (I $3d_{5/2}$) obtained at the "dark brown" spot from the cross section. C) Neutron radiograph of the postmortem battery cell containing carbon felt (marked with red-dashed line) at the bottom. The grayscale bar represents the transmittance value. D) Transmittance line scan along the orange line in (C).

presence of carbon felt can be easily recognized (marked with a red dashed line in Figure 4C, also see Figure S6, Supporting Information, for raw images). In contrast, the porous structure (open porosity of 95%) of the felt in the salt mixture leads to a darker contrast in the area L_2 compared to the graphite crucible due to more neutron opaque salt within the felt. By knowing the neutron attenuation coefficients and the densities of the used compounds, it is possible to evaluate the segregation of elements in the postmortem cell. The coefficients[75] and densities of the elements (when solid), together with the molar fraction, are given in **Table 2**. The neutron image clearly reveals an inhomogeneous distribution of elements based on the transmittance. The line scan (orange line in Figure 4C) of transmittance values presented in Figure 4D shows the possible segregation of a denser element with a lower neutron attenuation value while a less dense but more neutron-opaque element remains at the top. This is evident

by the observable gradient in part L_2 and strongly corresponds to the expected behavior of iodine. The concentration of iodine increases along the felt culminating in a larger cluster at the bottom part of the felt (potentially similar to the dark brown spot in Figure 4A). This confirms the visual evidence presented in Figure S5A, Supporting Information, as well as the predicted working principles of the cell.

The results obtained from postmortem analysis indicate the possibility of an iodine-concentrated layer that is formed during the charging process in the battery. Nonetheless, because the physical and chemical state of the salt can change during the cooling process, more direct evidence is necessary to confirm the presence of the iodine-concentrated layer, for instance, via *in situ* investigation.

2.6. Degradation and Long-Term Performance

Earlier, we suggested that the redox shuttling of iodide could be a possible contribution to the reduction in Coulombic efficiency, in particular, for deep charging/discharging cycles (Figure 3A). In fact, the low Coulombic efficiency also implies irreversible reactions, which are often responsible for performance degradation of batteries in general, such as capacity loss and increase in cell resistance. The latter, for instance, was reported for the Na||NaI–AlBr$_3$ battery, as evidenced by a noticeable performance change in terms of voltage and energy efficiency.[31,33] For investigating this aspect, one A-AI battery cell was assembled with the same cell configuration applied earlier for testing

Table 2. Attenuation coefficients for thermal neutrons, density, and molar fraction of the elements used in the cell.

Element	Neutron attenuation coefficient[75] [cm^{-1}]	Density [g cm^{-3}]	Molar fraction [%]
Li	3.30	0.53	31.5
I	0.23	4.93	47.5
Cl	1.33	1.56	2.5
K	0.06	0.89	4.5
Cs	0.29	1.93	14.0

ADVANCED
SCIENCE NEWS
www.advancedsciencenews.com

Energy Technology
Generation, Conversion, Storage, Distribution

www.entechnol.de

self-discharging performance. Then, the cell was charged and discharged at 50 mA cm^{-2} for 150 cycles and 100 mA cm^{-2} for further 100 cycles (**Figure 5**). For this test, the charging was limited to 73.8 mAh (2.5 mAhg), and the low cutoff voltage was set to 2 V. This test configuration does not reflect the full-range operation of batteries for maximum energy-storage capacity. Nonetheless, this type of test has often been applied to other molten-salt batteries for investigating various aspects of performance degradation by evaluating voltage, energy, and Coulombic efficiencies; in particular, for prototype cells without optimized cell configurations.[27,31,33] In prototype cells, a huge and ineffective volume of the electrolyte is often unavoidable. Since the charging capacity was fixed, the discharging capacity in Figure 5A represents Coulombic efficiency (Figure 5B), and the shape of the voltage profiles is closely related to the energy efficiency (Figure 5C). After a couple of initial cycles, the Coulombic and energy efficiency values became stabilized to around 87% and 76%, respectively. This initial change is also in line with the change in the voltage profile from the first to the twentieth cycle (Figure 5A). Particularly, the reduction in ohmic (iR)-drop indicates an improvement of cell resistance during the initial cycles (Figure 5B); in our case, the iR-drop was measured 1 s after applying a resting period of 3 s between the charging and discharging step. For the first 150 cycles, the iR-drop had been further decreased until a steady value of 0.11 V was reached. The Nyquist plots (Figure 5D) obtained

before and after 150 cycles are also in line with the decreasing tendency of iR-drop and indicate the improvement of impedance in the cell system. Electrochemical impedance spectroscopy was applied at 2 V with an amplitude of 5 mV in the frequency range of 1 MHz - 40 mHz. In the absence of detailed analysis with half-cell configurations for both anode and cathode compartments, the origin of these initial changes is not entirely clear at this moment. One of the possible reasons is the change in wetting behavior. Most probably, the wetting of the anode current collector improved during the initial cycles. Moreover, the wetting of molten salt in carbon felt could have been improved at the same time. Such change in wettability in porous carbon has been reported in aqueous energy-storage systems.[76,77]

After about 70 cycles at 50 mA cm^{-2}, the performance of the battery cell in terms of energy and Coulombic efficiency briefly degraded, followed by a quick stabilization (Figure 5B). This behavior can be explained by analyzing the voltage profiles in detail for the 80th and 149th cycles (Figure 5A). The major difference between these profiles is the length of the discharging period. The exact reason for this difference is unclear at this moment without further investigations. However, it may be related to the wetting behavior of the molten salt to the carbon felt since it influences the diffusion properties. Perhaps, the diffusion in the carbon felt might have been enhanced via the improved wetting, which led to the shortened tail for the concentration polarization as well as the increased self-discharging rate
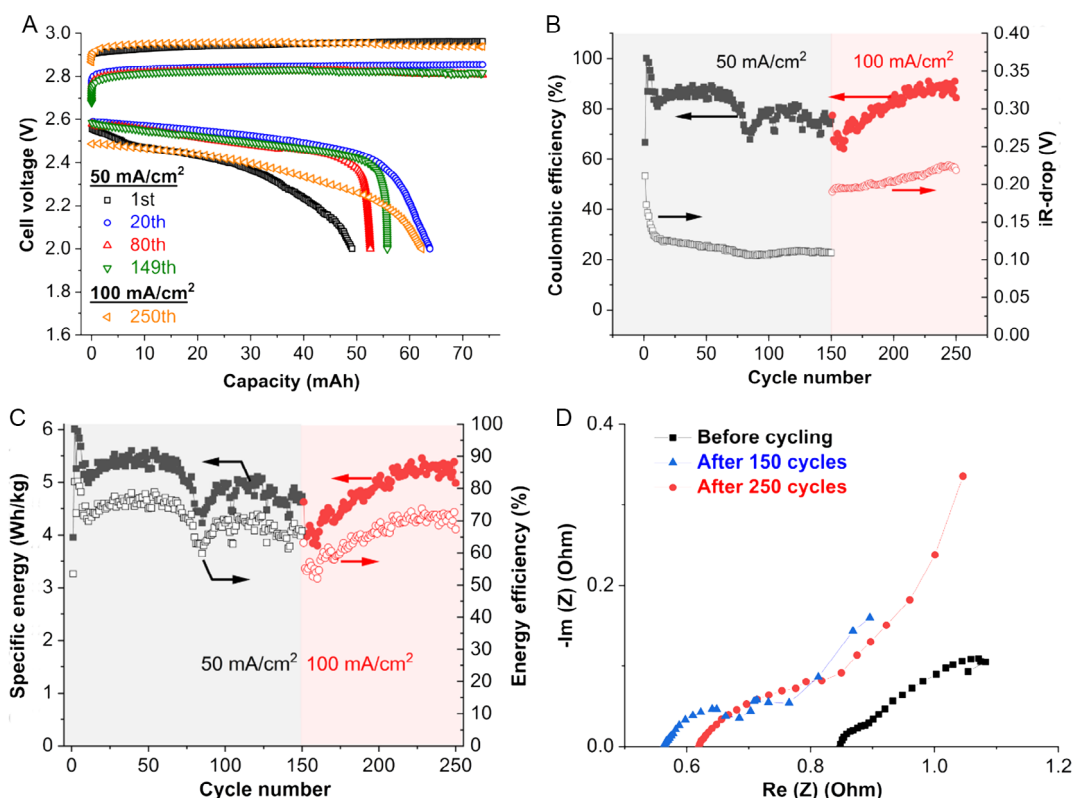

Figure 5. Electrochemical stability analysis for membrane-free A-Al batteries with LiI–LiCl–KI–CsI. A) Cell voltage profiles at various cycles. B) Coulombic efficiency and iR-drop, and C) specific energy and energy efficiency values as a function of cycle number. D) Nyquist plots obtained at various cycles. All results are obtained in the closed-cell configuration.

**ADVANCED
SCIENCE NEWS**

www.advancedsciencenews.com

Energy Technology
Generation, Conversion, Storage, Distribution

www.entechnol.de

through redox shuttling. The latter aspect is further supported by increased Coulombic efficiency at $100\,mA\,cm^{-2}$ for further 100 cycles (Figure 5B) because the period of the charging/discharging cycle is reduced by increased current density. During these additional cycles at $100\,mA\,cm^{-2}$, the iR-drop was slightly increased from 0.19 to 0.22 V, corresponding to the Nyquist plot obtained after 250 cycles (Figure 5D). Based on the increased intercept value on the x-axis, which is often referred as equivalent series resistance, it can be concluded that the electrical and/or ionic conductivity got slightly worsened after 250 cycles. The possible reasons could be the corrosion of the carbon felt, blockage of the porous network via the formation of the solid-state products due to side reactions, and loss of electrolyte and/or alkali metals via undesired reactions. All kind of side reactions or material loss will alter the electrolyte composition and influence thereby self-discharge. Any kind of fluid flow, especially caused by thermal convection, will have an influence on self-discharge and the Coulombic efficiency, too.[78] Despite everything, the investigated cell showed a stable performance for 250 cycles with a slight performance fluctuation in terms of energy and Coulombic efficiency, yet without a significant change in cell resistance except for the initial improvement.

3. Conclusions

As a proof-of-concept study, we demonstrated the performance of membrane-free A-AI batteries as a new type of energy-storage system. By employing LiI–LiCl–KI–CsI molten salt mixture, the A-AI batteries were successfully operated in the temperature range of 240–300 °C. The tested A-AI batteries provided a cell voltage of around 2.7 V and showed high power handling performance, as demonstrated by a voltage efficiency of 40% at $500\,mA\,cm^{-2}$. Despite the membrane-free configuration, a relatively low self-discharge rate of $3.56\,mA\,cm^{-2}$ was observed, which led to a maximum specific energy of $34.2\,Wh\,kg^{-1}$ with an energy efficiency of 59% for a charging/discharging period of 5.8 h. This result indicates that the A-AI batteries can be applied as stationary energy-storage systems for shaving three major peaks in electricity during a day. By optimizing current collectors and by employing porous separators or filler materials between the anode and cathode compartments, the self-discharge rate, power handling, and energy-storage performance of A-AI batteries can be further improved.

The postmortem analyses with neutron radiography and XPS implies the possibility of an iodine-concentrated layer, which could be generated at the bottom of the cell during the charging process. The presence of this layer could be responsible for the relatively low self-discharge rate observed in this study. However, concerning the limitation of postmortem analysis, follow-up studies are highly recommended, for instance, by various *in situ* approaches. Our prototype A-AI battery cell demonstrated a stable performance for 250 cycles in terms of energy and Coulombic efficiency with a slight fluctuation, and no particular increase in cell resistance. Since the stability test was carried out for shallow charging/discharging cycles due to the unoptimized cell design, a rigorous stability test including deep charging/discharging cycles at the various current densities will be necessary for future studies.

4. Experimental Section

Materials: The salt mixtures were prepared in a glove box filled with argon gas ($H_2O < 0.1$ ppm, $O_2 < 0.1$ ppm) with various molar ratios of LiI (99.95% purity, VladaChem), LiCl (99.995% purity, Alfa Aesar), KI (99.5% purity, Sigma Aldrich), and CsI (99.99% purity, chemPUR). A sheath out of boron nitride (HeBoSint D100, Henze Boron Nitride Products AG) and a cylindrical crucible out of glassy carbon (GAZ03, Sigradur) were used as cell components as received. Carbon felts (GFA 6.0 from SGL Carbon, 6 mm thickness) and Ni wires (0.5 mm diameter, 99.98% purity, Alfa Aesar) were applied as current collectors. The carbon felts were dried at 120 °C in a vacuum oven over 24 h and transported directly to the glove box while they were still warm.

Electrochemical Characterizations: The battery performance of the membrane-free A-AI batteries has been characterized by an SP-150 potentiostat/galvanostat (BioLogic) in a glove box filled with argon gas ($H_2O < 0.1$ ppm, $O_2 < 0.1$ ppm). For the characterizations, two different types of custom-built battery cells were assembled in the glove box: one closed cell (sealed) and one open cell with an opening on the top exposed to the argon environment (see Figure S1, Supporting Information). **Table 3** gives an overview on both cell types. For the open-cell characterization, the LiI–LiCl–KI–CsI electrolyte of ≈7 g was dried at 150 °C overnight in a crucible with a cylindrical shape consisting of glassy carbon at the bottom and an Al_2O_3 ceramic wall. The glassy carbon at the bottom of the crucible worked as a current collector at the cathode compartment with an exposed area of 1.3 cm^2 to the electrolyte. Prior to the experiments, an anode current collector out of nickel wire (0.5 mm diameter) with a circular flat spiral geometry (see Figure S1B, Supporting Information) was immersed into the molten salt after 1 h of resting time at 240 °C; the surface area of the nickel current collector exposed to the molten salt was about 1 cm^2. Additionally, a second nickel wire (0.5 mm diameter) with an Al_2O_3 ceramic sheath was also immersed (see Figure S1D, Supporting Information), located between the cathode and anode current collectors, and served as a quasi-reference electrode (QRE).[79–81]

In the case of the closed cell, the LiI–LiCl–KI–CsI electrolyte of ≈39 g with a molar ratio of 58:5:9:28 was dried at 150 °C overnight in a cylindrical glassy carbon crucible with an inner diameter of 30 mm. After heating and holding the temperature of the crucible at 240 °C for 1 h, the carbon felt with a circular shape having a diameter of 30 mm was immersed with the aid of the tube out of boron nitride. The boron nitride sheath had an inner diameter of 24 mm and an outer diameter of 30 mm. Inside the cell, the ceramic sheath naturally pressed the carbon felt when the cylindrical cell body out of steel (AISI 304) was sealed by a flanged lid. The sealing was secured by a ring-shaped copper gasket, and the feedthrough in the middle of the flange enabled electrical contact between the potentiostat/galvanostat and the nickel current collector; the latter was prepared by winding a 6 cm long nickel band with a width of 0.6 cm (see Figure S1, Supporting Information). For the characterization, the carbon felt was linked to the cathode terminal via the contact with the glassy carbon crucible and the contact between the glassy carbon and the steel body. The nickel current collector was linked directly to the anode terminal via the feedthrough out of nickel.

Phase Diagram Simulation with FactSage: The phase diagrams of the LiI–LiCl–KI–CsI system were simulated with the calculation of phase diagrams (CALPHAD) approach using FactSage (v. 8.0).[82,83] To estimate the

Table 3. Setup of the two investigated cell types.

	"Open" cell	"Closed" cell
Anode current collector	Ni spiral	Ni spiral
Cathode current collector	Glassy carbon	Carbon felt
Lateral insulation	Al_2O_3	Boron nitride
Electrolyte: LiI–LiCl–KI–CsI [mol%]	58:5:9:28 and 54:10:9:29	58:5:9:28
"Active" diameter [mm]	13	24

2300051 (9 of 12)

salt composition with the lowest melting temperature, the ternary phase diagrams were calculated under a constant LiCl molar fraction (0, 5, and 10 mol%). The estimated minimum melting temperature (below 200 °C) is the lowest for the LiI–LiCl–KI–CsI system with a composition of 58:5:9:28 mol%.

DSC: The Heat flux DSC 204 F1 Phoenix (NETZSCH) was used to verify the melting temperatures of the eutectic salt mixtures estimated by FactSage that are, LiI–LiCl–KI–CsI 60:0:10:30, 58:5:9:28, and 54:10:9:27 mol%. The salt mixtures were prepared in the glove box to avoid the hydration of the salt. About 10 mg of synthesized salt sample was filled into a gold-plated stainless-steel sealed crucible and analyzed by DSC. The sample was heated from 30 to 400 °C with a heating rate of 5 K min^{-1} and cooled down to room temperature with a cooling rate of 5 K min^{-1}.

Postmortem Analysis: For the postmortem analysis by neutron radiography and X-ray photoemission spectroscopy (XPS), a cylindrical graphite crucible (see Figure S5, Supporting Information) was filled with the molten LiI–LiCl–KI–CsI (58:5:9:28 mol%) mixture, and a nickel wire with a circular flat spiral geometry was immersed; the exposed area of the latter to the electrolyte was of 1.3 cm^2. Two postmortem cells were prepared, one with carbon felt located at the bottom part of the cell and one without. The graphite crucible had an inner diameter of 25.4 mm and an outer diameter of 31.7 mm. The bottom part of the crucible had a conical geometry; the depth of the middle part from the top was 20 mm, and the depth of the edge part from the top was 15.4 mm. Hence, after introducing the graphite felt with a thickness of 6 mm, there was a gap with a conical shape between the felt and the bottom part of the crucible. The cells were charged up to 100 mAh at 240 °C, rested for 1 h, and cooled naturally in the glove box up to a temperature around 30 °C.

The neutron radiographs were obtained at the beamline neutron transmission radiography (NEUTRA)[84] of the Swiss Spallation Neutron Source SINQ[85] at the Paul Scherrer Institute with a configuration reported elsewhere;[86,87] during the experiments, the proton beam current was 1.34 mA. The NEUTRA beamline was operated with a constant beam aperture of 20 mm, leading to ≈1.3×10^7 n cm^{-2} s^{-1} thermal neutron flux of 25 meV mean energy. The distance between the beam-defining 20 mm circular aperture and the scintillator screen (Gadolinium oxysulfide Gd$_2$O$_2$S: Tb, 40 μm thick) was 7292 mm, and the postmortem cell was located directly next to the scintillator. The images were obtained with an exposure time of 10 s. Sequences of five neutron radiographs were acquired by an sCMOS camera (Hamamatsu ORCA Flash 4.0, equipped with a photographic lens Nikon AF-S NIKKOR 50 mm 1:1.4 G) for a field of view (122 × 122 mm) with a 2048 × 2048 pixel array. In addition to the sample images of the postmortem cell, dark current and open beam images were acquired under the same imaging conditions. The recorded images were further processed using the open-source software Fiji. First, the selective median filter Remove Outliers was applied to remove bright and dark pixel-sized outliers. Subsequently, dark current and open beam images were averaged for each sample. Finally, image normalization was performed by dividing the dark current corrected sample image by the dark current corrected open beam image.

XPS was carried out using an ESCALAB 250Xi by Thermo Scientific with an XR6 monochromated Al Kα source ($h\nu = 1486.6$ eV), a spot size of 650 μm, and a pass energy of 20 eV. A flood gun was used for charge compensation. The sample was stored in the entry chamber of the ESCALAB 250Xi (base pressure: 2×10^{-8} mbar) for about 15 h before transferring it to the ultrahigh vacuum chamber (base pressure: 2×10^{-10} mbar) for measurements. To study the difference in composition throughout the battery, six points in a straight line from the bottom to the top of the sample, separated by a distance of approximately 2.4 mm, were analyzed. In addition, other specific areas of interest were analyzed as well, like the dark spots in the middle and the upper part of the sample (see *Supporting Information*, Figure S5D). The binding energies of the obtained spectrums were shifted based on the C1s peak as a reference, which was located at 284.8 eV. The fitting and deconvolution of the spectrum in the specific components, the chemical states, and the calculation of atomic composition were carried out employing the Avantage software provided by Thermo Scientific.

Supporting Information

Supporting Information is available from the Wiley Online Library or from the author.

Acknowledgements

Conflict of Interest

The authors declare no conflict of interest.

Data Availability Statement

The data that support the findings of this study are openly available at https://doi.org/10.14278/rodare.2192.

Keywords

[1] J. Xiang, L. Yang, L. Yuan, K. Yuan, Y. Zhang, Y. Huang, J. Lin, F. Pan, Y. Huang, *Joule* **2019**, *3*, 2334.

[2] H. Liu, X.-B. Cheng, Z. Jin, R. Zhang, G. Wang, L.-Q. Chen, Q.-B. Liu, J.-Q. Huang, Q. Zhang, *Energy Chem.* **2019**, *1*, 100003.

[3] J. Lu, Z. Chen, F. Pan, Y. Cui, K. Amine, *Electrochem. Energy Rev.* **2018**, *1*, 35.

[4] J. W. Choi, D. Aurbach, *Nat. Rev. Mater.* **2016**, *1*, 1.

[5] S. Wang, R. Fang, Y. Li, Y. Liu, C. Xin, F. H. Richter, C.-W. Nan, *J. Mater.* **2021**, *7*, 209.

[6] N. Boaretto, I. Garbayo, *J. Power Sources* **2021**, *502*, 229919.

[7] Q. Ma, F. Tietz, *ChemElectroChem* **2020**, *7*, 2693.

[8] Q. Zhao, S. Stalin, C.-Z. Zhao, L. A. Archer, *Nat. Rev. Mater.* **2020**, *5*, 229.

[9] H. Li, H. Yin, K. Wang, S. Cheng, K. Jiang, D. R. Sadoway, *Adv. Energy Mater.* **2016**, *6*, 1600483.

[10] H. Kim, D. A. Boysen, J. M. Newhouse, B. L. Spatocco, B. Chung, P. J. Burke, D. J. Bradwell, K. Jiang, A. A. Tomaszowska, K. Wang, W. Wei, L. A. Ortiz, S. A. Barriga, S. M. Poizeau, D. R. Sadoway, *Chem. Rev.* **2013**, *113*, 2075.

[11] X.-B. Cheng, R. Zhang, C.-Z. Zhao, Q. Zhang, *Chem. Rev.* **2017**, *117*, 10403.

[12] D. Swinkels, in *Advances in Molten Salt Chemistry*, Springer, New York **1971**, pp. 165–223.

[13] R. D. Weaver, S. W. Smith, N. L. Willmann, *J. Electrochem. Soc.* **1962**, *109*, 653.

[14] E. J. Cairns, H. Shimotake, *Science* **1969**, *164*, 1347.

[15] C.-H. Dustmann, *J. Power Sources* **2004**, *127*, 85.

[16] W. Yu, K. C. Lau, Y. Lei, R. Liu, L. Qin, W. Yang, B. Li, L. A. Curtiss, D. Zhai, F. Kang, *ACS Appl. Mater. Interfaces* **2017**, *9*, 31871.

[17] Y. Zhang, J. Lou, Y. Shuai, K. Chen, X. He, Y. Wang, N. Li, Z. Zhang, F. Gan, *Mater. Lett.* **2019**, *242*, 5.

[18] H. Li, K. Wang, H. Zhou, X. Guo, S. Cheng, K. Jiang, *Energy Storage Mater.* **2018**, *14*, 267.

[19] K. B. Hueso, M. Armand, T. Rojo, *Energy Environ. Sci.* **2013**, *6*, 734.

[20] D. Kumar, S. K. Rajouria, S. B. Kuhar, D. K. Kanchan, *Solid State Ion.* **2017**, *312*, 8.

[21] A. Vanzyl, *Solid State Ion.* **1996**, *86–88*, 883.

[22] P. Parthasarathy, N. Weber, A. V. Virkar, *ECS Trans.* **2007**, *6*, 67.

[23] X. Lu, G. Li, J. Y. Kim, J. P. Lemmon, V. L. Sprenkle, Z. Yang, *Energy Environ. Sci.* **2013**, *6*, 1837.

[24] J. Xu, O. S. Kjos, K. S. Osen, A. M. Martinez, O. E. Kongstein, G. M. Haarberg, *J. Power Sources* **2016**, *332*, 274.

[25] J. Xu, A. M. Martinez, K. S. Osen, O. S. Kjos, O. E. Kongstein, G. M. Haarberg, *J. Electrochem. Soc.* **2017**, *164*, A2335.

[26] B. H. Chung, D. R. Sadoway US 2014/0272481 A1, **2018**.

[27] H. Yin, B. Chung, F. Chen, T. Ouchi, J. Zhao, N. Tanaka, D. R. Sadoway, *Nat. Energy* **2018**, *3*, 127.

[28] K. Mushtaq, J. Zhao, N. Weber, A. Mendes, D. R. Sadoway, *J. Energy Chem.* **2022**, *66*, 390.

[29] D. E. Glass, J.-P. Jones, A. V. Shevade, D. Bhakta, E. Raub, R. Sim, R. V. Bugga, *J. Power Sources* **2020**, *449*, 227492.

[30] E. D. Spoerke, S. Percival, L. J. Small, US 2021/0075059 A1, **2021**.

[31] M. M. Gross, S. J. Percival, L. J. Small, J. Lamb, A. S. Peretti, E. D. Spoerke, *ACS. Appl, Energy Mater.* **2020**, *3*, 11456.

[32] S. J. Percival, L. J. Small, E. D. Spoerke, *J. Electrochem. Soc.* **2018**, *165*, A3531.

[33] L. J. Small, A. Eccleston, J. Lamb, A. C. Read, M. Robins, T. Meaders, D. Ingersoll, P. G. Clem, S. Bhavaraju, E. D. Spoerke, *J. Power Sources* **2017**, *360*, 569.

[34] Q. Gong, W. Ding, A. Bonk, H. Li, K. Wang, A. Jianu, A. Weisenburger, A. Bund, T. Bauer, *J. Power Sources* **2020**, *475*, 228674.

[35] R. A. Guidotti, F. W. Reinhardt, J. Odinek, *J. Power Sources* **2004**, *136*, 257.

[36] R. C. Vogel, L. Burris, A. D. Tevebaugh, D. S. Webster, E. R. Proud, Tech. Rep. ANL-7650., Argonne National Laboratory, **1969**.

[37] J. Lee, P. Srimuk, S. Fleischmann, X. Su, T. A. Hatton, V. Presser, *Prog. Mater Sci.* **2019**, *101*, 46.

[38] J. Lee, P. Srimuk, R. L. Zornitta, M. Aslan, B. L. Mehdi, V. Presser, *ACS Sustain. Chem. Eng.* **2019**, *7*, 10132.

[39] J. Lee, B. Krüner, A. Tolosa, S. Sathyamoorthi, D. Kim, S. Choudhury, K.-H. Seo, V. Presser, *Energy Environ. Sci.* **2016**, *9*, 3392.

[40] J. Lee, P. Srimuk, S. Carpier, J. Choi, R. L. Zornitta, C. Kim, M. Aslan, V. Presser, *ChemSusChem* **2018**, *11*, 3460.

[41] J. Lee, P. Srimuk, S. Fleischmann, A. Ridder, M. Zeiger, V. Presser, *J. Mater. Chem. A* **2017**, *5*, 12520.

[42] B. Li, Z. Nie, M. Vijayakumar, G. Li, J. Liu, V. Sprenkle, W. Wang, *Nat. Commun.* **2015**, *6*, 6303.

[43] C. Prehal, H. Fitzek, G. Kothleitner, V. Presser, B. Gollas, S. A. Freunberger, Q. Abbas, *Nat. Commun.* **2020**, *11*, 4838.

[44] R. P. Akkermans, Q. Fulian, S. L. Roberts, M. F. Suárez, R. G. Compton, *J. Phys. Chem. B*, **1999**, *103*, 8319.

[45] L. M. Dané, L. J. J. Janssen, J. G. Hoogland, *Electrochim. Acta* **1968**, *13*, 507.

[46] P. H. Svensson, L. Kloo, *Chem. Rev.* **2003**, *103*, 1649.

[47] H. Stegemann, A. Rohde, A. Reiche, A. Schnittke, H. Füllbier, *Electrochim. Acta* **1992**, *37*, 379.

[48] S. P. Kelley, H. Pei, V. Smetana, A.-V. Mudring, R. D. Rogers, *Cryst. Growth Des.* **2020**, *20*, 498.

[49] S. Bénard, N. Weber, G. M. Horstmann, S. Landgraf, T. Weier, *J. Power Sources* **2021**, *510*, 230339.

[50] D. H. Kelley, D. R. Sadoway, *Phys. Fluids* **2014**, *26*, 057102.

[51] Y. Shen, O. Zikanov, *Theor. Comput. Fluid Dyn.* **2016**, *30*, 275.

[52] P. Personnettaz, S. Landgraf, M. Nimtz, N. Weber, T. Weier, *Electrochem. Commun.* **2019**, *105*, 106496.

[53] T. Ouchi, H. Kim, B. L. Spatocco, D. R. Sadoway, *Nat. Commun.* **2016**, *7*, 10999.

[54] A. Z. Weber, M. M. Mench, J. P. Meyers, P. N. Ross, J. T. Gostick, Q. Liu, *J. Appl, Electrochem.* **2011**, *41*, 1137.

[55] J.-S. Yeo, E. Yoo, C. N. Im, J.-H. Cho, *Electrochim. Acta* **2021**, *389*, 138697.

[56] J.-S. Yeo, J.-H. Lee, E.-J. Yoo, *Electrochim. Acta* **2018**, *290*, 228.

[57] J. Kim, D. Shin, Y. Jung, S. M. Hwang, T. Song, Y. Kim, U. Paik, *J. Power Sources*, **2018**, *377*, 87.

[58] M. Uddin, M. F. Romlie, M. F. Abdullah, S. Abd Halim, A. H. Abu Bakar, T. Chia Kwang, *Renew. Sustain. Energy Rev.*, **2018**, *82*, 3323.

[59] E. Cairns, C. Crouthamel, A. Fischer, M. Foster, J. Hesson, C. Johnson, H. Shimotake, A. Tevebaugh, ANL-7316, Argonne National Laboratory 1967.

[60] B. L. Spatocco, T. Ouchi, G. Lambotte, P. J. Burke, D. R. Sadoway, *J. Electrochem, Soc.* **2015**, *162*, A2729.

[61] D. J. Bradwell, H. Kim, A. H. C. Sirk, D. R. Sadoway, *J. Am. Chem. Soc.* **2012**, *134*, 1895–1897.

[62] A. Dworkin, H. Bronstein, M. Bredig, *J. Phys. Chem.* **1962**, *66*, 572.

[63] B. Evanko, S. W. Boettcher, S. J. Yoo, G. D. Stucky, *ACS Energy Lett.* **2017**, *2*, 2581.

[64] D. H. Kelley, T. Weier, *Appl. Mech. Rev.* **2018**, *70*, 020801.

[65] R. F. Ashour, D. H. Kelley, A. Salas, M. Starace, N. Weber, T. Weier, *J. Power Sources* **2018**, *378*, 301.

[66] N. Weber, M. Nimtz, P. Personnettaz, T. Weier, D. Sadoway, *J. Power Sources Adv.*, **2020**, *1*, 100004.

[67] W. Herreman, C. Nore, L. Cappanera, J. L. Guermond, *J. Fluid Mech.* **2021**, *915*, A17.

[68] T. Köllner, T. Boeck, J. Schumacher, *Phys. Rev. E* **2017**, *95*, 053114.

[69] R. J. Magaa, J. S. Lannin, *Phys. Rev. B Condens. Matter Mater. Phys.* **1985**, *32*, 3819.

[70] G. J. Janz, F. W. Dampier, G. R. Lakshminarayanan, P. K. Lorenz, R. P. T. Tomkins, in *Molten Salts: Volume 1, Electrical Conductance, Density, and Viscosity Data*, NIST (National Bureau of Standards), Gaithersburg, Maryland **1968**.

[71] W. Herreman, S. Bénard, C. Nore, P. Personnettaz, L. Cappanera, J. L. Guermond, *Phys. Rev. Fluids* **2020**, *5*, 074501.

[72] P. Personnettaz, S. Landgraf, M. Nimtz, N. Weber, T. Weier, *Magnetohydrodynamics* **2020**, *56*, 247.

[73] P. Personnettaz, T. S. Klopper, N. Weber, T. Weier, *Heat Mass Transfer* **2022**, *188*, 122555.

[74] T. G. Levitskaia, S. Chatterjee, B. W. Arey, E. L. Campbell, Y. Hong, L. Kovarik, J. M. Peterson, N. K. Pence, J. Romero, V. Shutthanandan, B. Schwenzer, T. Varga, *RSC Adv.* **2016**, *6*, 76042.

[75] NIST Center for Neutron Research, Neutron Activation and Scattering Calculator, NIST Center for Neutron Research.

[76] J. Lee, D. Weingarth, I. Grobelsek, V. Presser, *Energy Technol.* **2016**, *4*, 75.

[77] K. Fic, G. Lota, E. Frackowiak, *Electrochim. Acta* **2010**, *55*, 7484.

[78] C. Duczek, N. Weber, O. E. Godinez-Brizuela, T. Weier, *Electrochim. Acta* **2023**, *437*, 141413.

[79] J. Lee, N. Jäckel, D. Kim, M. Widmaier, S. Sathyamoorthi, P. Srimuk, C. Kim, S. Fleischmann, M. Zeiger, V. Presser, *Electrochim. Acta* **2016**, *222*, 1800.

**ADVANCED
SCIENCE NEWS**

www.advancedsciencenews.com

Energy Technology
Generation, Conversion, Storage, Distribution

www.entechnol.de

[80] D. Weingarth, A. Foelske-Schmitz, A. Wokaun, R. Kötz, *Electrochem. Commun.* **2012**, *18*, 116.

[81] I. Rivas, D. Puente, I. Ayerdi, E. Castano, in *Conf. on Electron Devices*, IEEE (Institute of Electrical and Electronics Engineers), Tarragona, Spain **2005**, pp. 465–468.

[82] C. W. Bale, P. Chartrand, S. A. Degterov, G. Eriksson, K. Hack, R. Ben Mahfoud, J. Melançon, A. D. Pelton, S. Petersen, *Calphad* **2002**, *26*, 189.

[83] B. Sundman, H. Lukas, S. Fries, in *Computational Thermodynamics: The Calphad Method*, Cambridge University Press, Cambridge **2007**.

[84] E. H. Lehmann, P. Vontobel, L. Wiezel, *Nondestr. Test. Eval.* **2001**, *16*, 191.

[85] B. Blau, K. N. Clausen, S. Gvasaliya, M. Janoschek, S. Janssen, L. Keller, B. Roessli, J. Schefer, P. Tregenna-Piggott, W. Wagner, O. Zaharko, *Neutron News* **2009**, *20*, 5.

[86] T. Lappan, M. Sarma, S. Heitkam, D. Mannes, P. Trtik, N. Shevchenko, K. Eckert, S. Eckert, in *Materials Processing Fundamentals* (Eds J. Lee, S. Wagstaff, A. Anderson, F. Tesfaye, G. Lambotte, A. Allanore) Springer, Cham **2021**, pp. 13–29.

[87] T. Lappan, M. Sarma, S. Heitkam, P. Trtik, D. Mannes, K. Eckert, S. Eckert, *Magnetohydrodynamics* **2020**, *56*, 167.